Proc. 3rd Int. Symp. on Turbulence and Shear Flow Phenomena, Sendai, June 2003

SPATIO-TEMPORAL EVOLUTION OF COHERENT VORTICES IN WALL TURBULENCE WITH STREAMLINE CURVATURE

Mitsuhiro Nagata, Nobuhide Kasagi
Department of Mechanical Engineering
The University of Tokyo
Hongo, Bunkyo-ku, Tokyo 113-8656, Japan
nagata@thtlab.t.u-tokyo.ac.jp

ABSTRACT

The effect of wall curvature on the turbulent structure in curved channel flow is investigated by means of direct numerical simulation (DNS). Four different radii of curvature, δ/Rc=0.013, 0.05, 0.1 and 0.2, are studied. The DNS results show: 1) reduction of turbulence intensities on the convex wall, and 2) increase of radial turbulence intensity in the central region of channel with the increase of curvature. It is revealed that such turbulence modulation is attributed to the extra production of the Reynolds stress caused by the centrifugal force. Moreover, a spatio-temporal LSE (Linear Stochastic estimation) is applied in order to extract the development of turbulence-producing eddies affected by centrifugal force. It is clarified that the development of turbulence-producing motion is associated with the large-scale strong roll-cell working against the centrifugal stabilizing effect on the convex side, whereas those vortices are not observed on the concave side. In addition, strong outward and inward motions induced by the roll cell in the channel central region appear prior to the development of second and fourth quadrant motions, respectively.

INTRODUCTION

Flow over a curved surface frequently appears in the industrial applications such as aerofoils, turbine cascades, pipe lines, and so on. In order to attain increased efficiency of fluidmachinery, it is very important to clarify the curved flow that involves inherent unstable and stable effects.

Experimental studies of wall turbulence subject to a streamline curvature were carried out, e.g., by Wattendorf (1935) and Eskinazy and Yeh (1956). In these investigations, the consideration is mainly restricted to the first-order statistics. On the other hand, direct numerical simulation conducted by Moser and Moin (1987) provides various statistics, but it only deals with 'weak' curvature. Therefore, the current knowledge on the dynamical mechanism affected by streamwise curvature still remains insufficient.

In this study, direct numerical simulation of fully developed turbulent curved channel flow is carried out to clarify the production and dissipation mechanisms near the convex and concave walls, and space-time linear stochastic estimation is employed to obtain the spatio-temporal evolution process of turbulence-producing eddies.

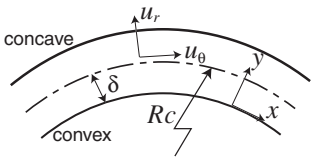

Fig. 1 Computational domain

Table 1 Computational condition

	δ/Rc	Re_τ
case 1	0.013	150
case 2	0.05	150
case 3	0.1	150
case 4	0.2	150

NUMERICAL METHOD

The Navier-Stokes equation is derived with the contravariant velocities through the coordinate transformation. A staggered grid system is adopted. The coupling between continuity and momentum equations is achieved through the fractional step method. The second order central difference scheme is used for spatial discretization and all the terms are advanced in time with the Crank-Nicolson method. The computational domain is shown in Fig. 1, where δ is the channel half-width and Rc is the radius of curvature at the channel center line. Four test cases are listed in Table 1. The computational domain is $2.5\pi\delta \times 2\delta \times \pi\delta$ in the streamwise, wall-normal and spanwise directions, respectively, and is covered 64x128x64 grid points. The no-slip condition about the velocity field and iso-heat flux condition about the temparature field are employed at the wall.

DNS OF TURBULENT CURVED CHANNEL FLOW

Friction Coefficient and Nusselt Number

The skin friction coefficient $C_f = 2\tau_w / \left(\rho \langle u_\theta \rangle^2\right)$ and the Nusselt number $Nu = 2hd / \lambda$, where $h = q_w / (T_w - [T])$, are shown as a function of the curvature in Fig. 2. Here, the bracket denotes the integral mean value from each wall to the maximum velocity point and C_{f0} and Nu_0 represent the values of the plane channel. As the curvature increases, the friction coefficient increases on the concave side due to the centrifugal instability effect, while it decreases on the convex side. The Nusselt number

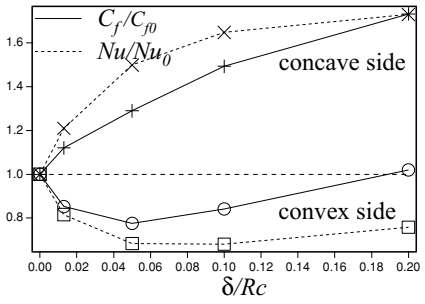

Fig. 2 C_f and Nu versus δ/Rc.

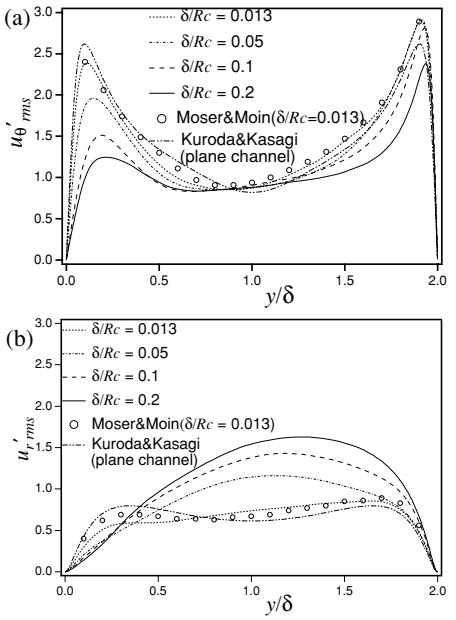

Fig. 3 Turbulence intensity distributions.
(a) streamwise component; (b) radial component.

shows a similar trend, but the rate of change is generally larger than that of the friction coefficient.

Figure 3 shows the rms turbulence fluctuation distributions. On the convex side, the streamwise turbulence intensity is noticeably reduced due to the stabilizing centrifugal effect. The radial turbulence intensity excels in the central region of channel with increasing the curvature. It eventually exceeds the streamwise component when the curvature is larger than 0.05.

Flux Richardson Number Distributions

The flux Richardson number, which is originally defined to represent the buoyancy effect in the stratified flow, is extended to the flow with streamline curvature (Bradshaw, 1969). This number is expressed by the ratio of the radial turbulence production by the centrifugal force to the streamwise turbulence shear production, i.e.,

$$R_f = \frac{2U_\theta / r}{r\partial(U_\theta / r)/\partial r}. \tag{1}$$

The streamwise and radial production terms are expressed as follows:

$$P_{\theta\theta} = -2\left(\overline{u_\theta u_r} r \frac{\partial(U_\theta / r)}{\partial r} + 2\overline{u_\theta u_r}\frac{U_\theta}{r}\right), \tag{2}$$

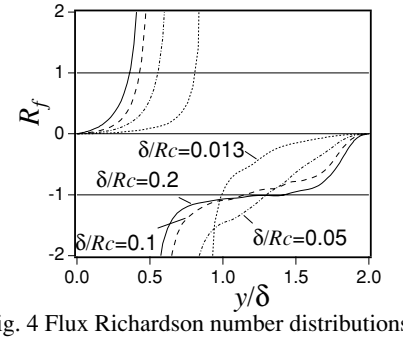

Fig. 4 Flux Richardson number distributions.

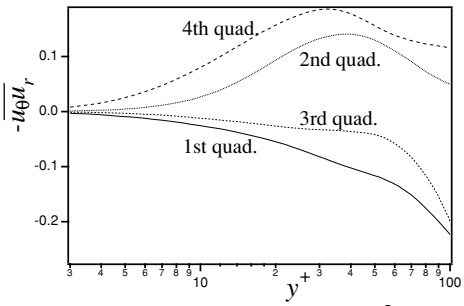

Fig. 5 Quadrant analysis on convex side (δ/Rc=0.05).

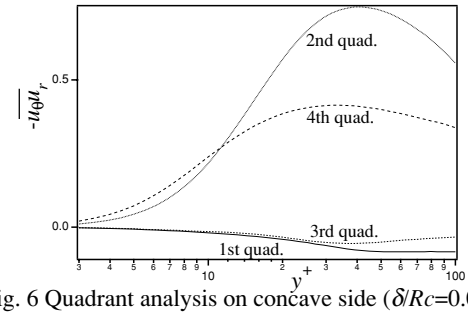

Fig. 6 Quadrant analysis on concave side (δ/Rc=0.05).

$$P_{rr} = 4\overline{u_\theta u_r}\frac{U_\theta}{r}. \tag{3}$$

The second term of Eq. (2) and Eq. (3) have the same absolute value with opposite signs. This implies the redistribution between streamwise and radial Reynolds stresses through the centrifugal effect. Therefore, the flux Richardson number also represents the ratio of redistribution to shear production. As shown in Fig. 4, R_f takes positive values on the convex side. Although this distribution implies the occurrence of redistribution from radial to streamwise direction, the effect is small. On the other hand, R_f takes negative values on the concave side. This is attributed to the energy flow from the streamwise to the radial directions. Especially, R_f is less than -1 in the channel central region when the curvature is larger than 0.05. This means that the energy flow from the streamwise to radial directions is larger than the shear production. Through this effect, the radial turbulence intensity excels as observed in Fig. 3(b).

Quadrant Analysis

The quadrant analysis of the Reynolds shear stress provides detailed information on the contribution of various combinations of positive and negative u_θ and u_r to the turbulent stress production. Figure 5 shows the quadrant analysis on the convex side when δ/Rc=0.05. We define y^+ as the local wall coordinate on the convex wall. The fourth quadrant is the main

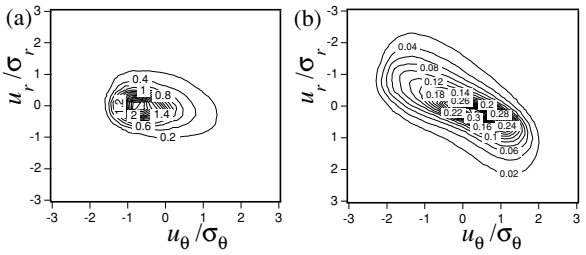

Fig. 7 Joint probability density function distribution at y^+=13. (a) convex side; (b) concave side (δ/Rc=0.05).

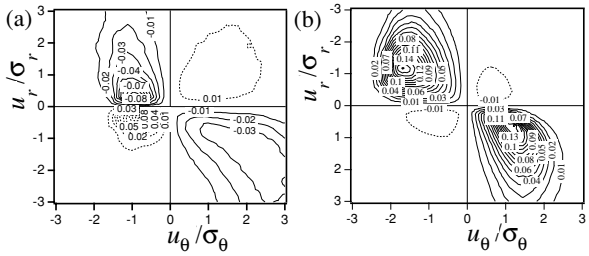

Fig. 8 Contribution to the Reynolds shear stress at y^+=13. (a) convex side ; (b) concave side (δ/Rc=0.05).

contributor to the Reynolds shear stress in the entire region on the convex side, and this fact indicates that on the stable side the turbulent motion is maintained by the inflow of high speed fluid. Figure 6 represents the quadrant analysis on the concave side. The fourth quadrant most contributes to the Reynolds shear stress only in the region of y^+<10, whereas the second quadrant acts as the main contributor in the other region. This trend is similar to that of plane channel. Moreover, on the convex side the contribution of the second and fourth quadrants has almost the same absolute value of that of first and third quadrants, whereas on the concave side the second and fourth quadrants contribute much greater than first and third quadrants. This trend is further investigated on the following section.

Joint Probability Density Function and Contribution to the Reynolds Shear Stress

Figure 7 shows the joint probability density function distribution with respect to the velocity fluctuations u_θ and u_r on the convex and concave walls. Here, the velocity fluctuations u_θ and u_r are normalized by their standard deviations. A distribution of elliptic form appears and definite correlation is scarcely seen on the convex side. In contrast, strong negative correlation appears on the concave side due to the high occurrence possibility of the second and fourth quadrant motion.

The contribution to the Reynolds shear stress, $u_\theta u_r f(u_\theta, u_r)$, on the convex and concave sides is shown in Fig. 8. Here, $f(u_\theta, u_r)$ is the joint PDF, and the following relationship holds:

$$\overline{u_\theta u_r} = \iint u_\theta u_r f(u_\theta, u_r) du_\theta du_r . \tag{4}$$

On the convex side (Fig. 8(a)), all the quadrants contribute to the Reynolds shear stress. Especially, large peaks are seen in the second and third quadrants. On the concave side, the distribution on the second and fourth quadrants is pronounced whereas the contributions from the first and third quadrants are diminished.

SPATIO-TEMPORAL LINEAR STOCHASTIC ESTIMATION

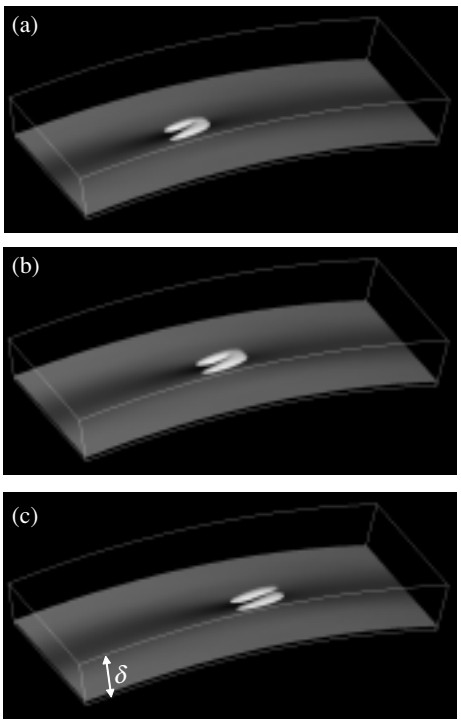

Fig. 9 Time development of the fourth quadrant vortices and high speed region on the convex side (δ/Rc=0.05). (a) τ^+=-10.5; (b)τ^+=0; (c)τ^+=10.5.

White, II^+=0.22x10^{-3}; gray contour, $\hat{u}_\theta$=-2.4 to 2.4 (y^+=10).

The Linear Stochastic Estimation (LSE) which is originally proposed by Adrian(1975) is a statistical estimation procedure of the representative flow structure for a given velocity condition around a sample point. In this study, this technique is extended to a spatio-temporal LSE for the purpose of extracting the development process of turbulence production eddies affected by the centrifugal force. Through this procedure, an estimated velocity field, $\hat{u}_i$, is represented by the velocity condition u_{cj} through the linear combination, i.e.,

$$\hat{u}_i(\mathbf{x}', \tau; \mathbf{x}, t) = A_{ij} u_{cj}(\mathbf{x}, t), \tag{5}$$

where $\mathbf{x}$ is the point where the velocity condition is imposed, $\mathbf{x}'$ is the location relative to $\mathbf{x}$, t is the time when the velocity condition is given and τ is the elapsed time from t. A location of y^+ =15 is adopted as the velocity condition point $\mathbf{x}$ and the velocities which have the maximum contribution to the second and fourth quadrants of Reynolds shear stress are used as the velocity conditions. The curvature, δ/Rc, is set to 0.05 in which the radial turbulent intensity becomes larger than the streamwise component (Fig. 3). The velocities that have the maximum contribution to the Reynolds shear stress are u_θ=-1.89, u_r=7.99x10^{-2} (second quadrant) and u_θ=2.45, u_r=-0.176 (fourth quadrant) on the convex side, whereas those are u_θ=-5.64, u_r=0.6 (second quadrant) and u_θ=-3.24, u_r=-0.2 (fourth quadrant) on the concave side.

The estimation coefficient A_{ij} in Eq. (7) is determined under the least square condition of the difference between the velocity obtained by the conditional averaging and that estimated by Eq.(7). According to this procedure, the coefficient A_{ij} is obtained from the space-time two point correlation of the velocity components.

Hereafter, we refer the movement induced by the second/fourth quadrant as second/fourth-quadrant motion.

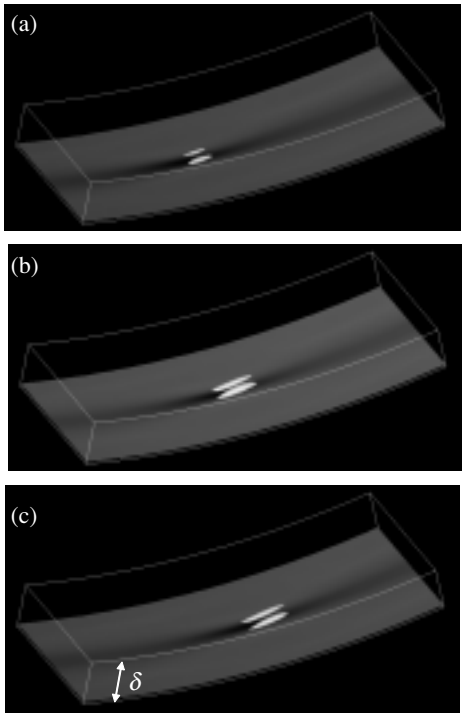

Fig. 10 Time development of the fourth quadrant vortices and high speed region on the concave side.
(a) τ^+=-10.5; (b) τ^+=0; (c) τ^+=10.5 (δ/Rc=0.05).
White, II$^+$=0.44x10^{-3}; gray contour, $\hat{u}_\theta$=-3.22 to 3.22 (y^+=10)

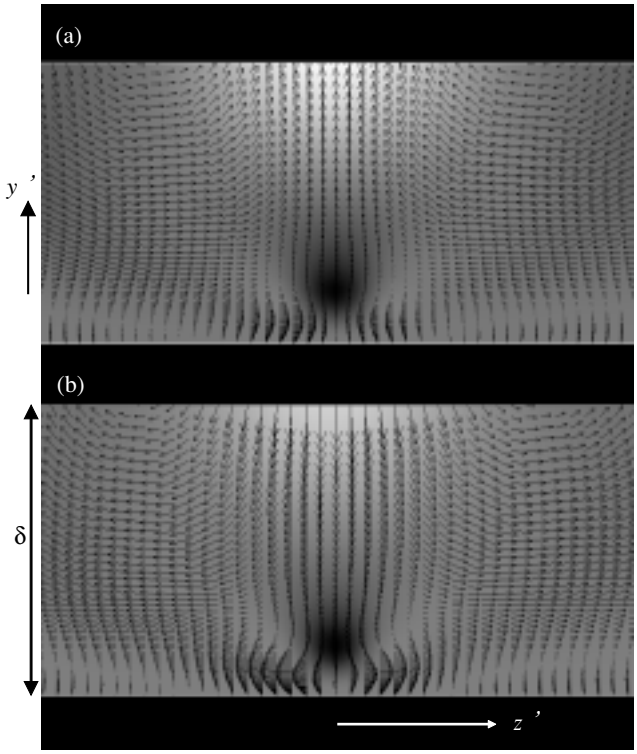

Fig. 11 Estimated velocity vector $\hat{u}_r, \hat{u}_z$ and Reynolds stress $\hat{u}_\theta \hat{u}_r$ contour on the convex side. (a) 2nd quadrant; (b) 4th quadrant; τ^+=0, x^+=0.

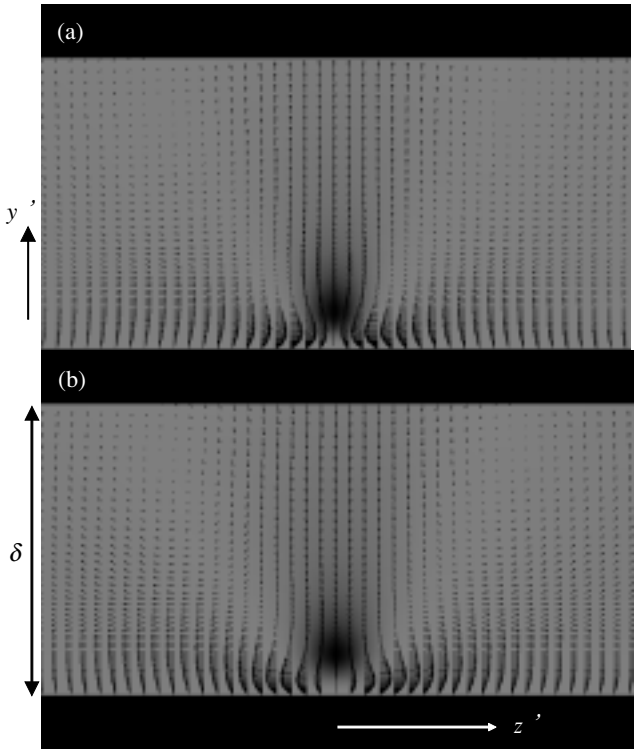

Fig. 12 Estimated velocity vector $\hat{u}_r, \hat{u}_z$ and Reynolds stress $\hat{u}_\theta \hat{u}_r$ contour on the concave side. (a) 2nd quadrant; (b) 4th quadrant; τ^+=0, x^+=0.

Time Development of the Turbulence Producing Eddies and High-Speed Region

Figure 9 shows the evolution of the fourth quadrant vortices and high speed region on the convex side. The vortices are identified by the second invariant of velocity deformation tensor II = $u_{i,j}u_{j,i}$. At τ^+=-10.5 (Fig. 9(a)), a hairpin-like vortex is detected and this structure is maintained until τ^+=0. After that, the vortex structure becomes a pair of streamwise vorticies as a consequence of the attenuation of the hairpin-head. This structure is convected further downstream with decaying. On the other hand, in the development of the fourth quadrant vortices on the concave side (Fig. 10), a pair of streamwise vortices is detected and this structure is developing toward τ^+=0. The estimated vortical structure at τ^+=0 remains as a pair of streamwise vortices. Furthermore, the high speed streak appears under the region between the streamwise vortices. As the time elapses, the pair of vortices becomes thinner while being convected downstream (Fig. 10(c)).

The Vortical Structure in the y'-z' Cross-section

Figure 11 shows the estimated velocity vectors and the Reynolds shear stress contour in the y'-z' cross-section (y':wall-normal direction; z':spanwise coordinate relative to the velocity condi0tion point) on the convex side at x'=0 and τ'=0. The upper edge of Fig. 11 corresponds to the channel center plane and the bottom edge to the convex wall. In the case of second quadrant (Fig. 11(a)), a strong Reynolds stress is induced around the point where the velocity condition is given. The second quadrant motion that is directed away from the wall is seen at the same point. A pair of large roll cells, which makes strong upward motion along z'=0, is additionally observed in the channel central region. This result suggests that a strong upward motion induced by the large organized vortices is required for

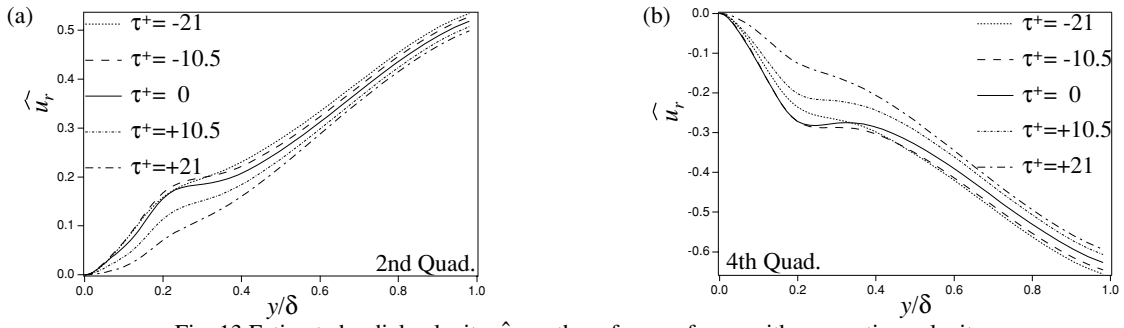

Fig. 13 Estimated radial velocity $\hat{u}_r$ on the reference frame with convective velocity.
(convex side, (a) 2nd quadrant; (b) 4th quadrant; x'=0 at τ=0, z'=0)

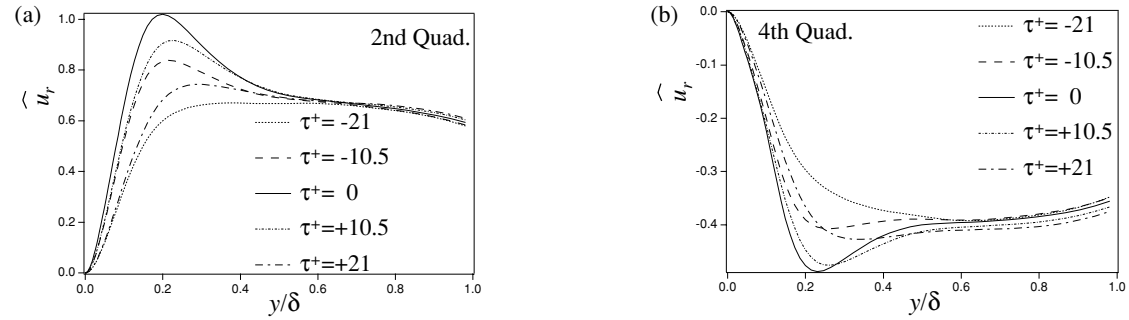

Fig. 14 Estimated radial velocity $\hat{u}_r$ on the reference frame with convective velocity
(concave side, (a) 2nd quadrant; (b) 4th quadrant; x'=0 at τ=0, z'=0)

the second quadrant motion to develop against the centrifugal stabilizing effect on the convex side.

A similar feature also appears in the case of fourth quadrant motion as shown in Fig. 11(b). In this case, the roll cell observed in the channel central region makes a strong downwash and this downward motion produces the fourth quadrant motion at the point where the velocity condition is given. Another interpretation is that the fourth quadrant motion is developed through the downwash induced by the roll cell on the convex wall.

Figure 12 shows the velocity vectors and Reynolds stress contour on the concave side. In the second quadrant motion (Fig.12(a)), a strong flow is induced from both sides of the spanwise direction to the velocity condition point and directed to the wall-normal direction. In contrast to the convex side, large roll cells are not observed near the channel central region. A similar flow pattern can be seen in the fourth quadrant motion (Fig. 12(b)). A strong flow is induced from the channel center region toward the velocity condition point along the axis of z'=0 and the fourth quadrant motion is produced at the velocity condition point. After that, the flow is directed to the both side of the spanwise direction. These two results suggest that the strong vortex motion (such as roll cell) is not required for the development of the second and fourth quadrant motion on the concave side, since there is an inherent self-sustaining mechanism which enhances the turbulent motion according to Fig. 8(b).

Time Development of the Estimated Velocity on the Reference Frame with Convective Velocity

In this section, we consider the time variation of the estimated velocity along z'=0 axis on the convex and concave sides. The estimated velocity is observed on the reference frame moving with the convective velocity. The frame is x'=0 at τ^+=0 and translates to the downstream direction with the convective velocity. The convective velocity is determined through the spatio-temporal two point correlation.

Figure 13(a) shows the time dependency of the estimated radial velocity distributions in the second quadrant motion. The radial velocity at the earliest time (τ^+ =-21) attains its maximum value in the channel middle region (y/δ~1.0) and monotonically decreases as the time elapses. It is conjectured that the second quadrant motion at τ^+=0 is induced due to the strong outflow in the channel middle region driven by the roll cell (Fig. 11(a)) at the prior time (τ^+<0). In accordance with that, the radial velocity in the near-wall region (y/δ~0.2) already retains high value at the prior time (τ^+<0), following the drastic decrease at τ^+>0 owing to the centrifugal stabilizing effect on the convex side.

The same tendency is seen in the fourth quadrant motion (Fig. 13(b)). The radial velocity $\hat{u}_r$ has maximum absolute value at the most previous time τ^+=-21 in the channel middle region and monotonically decreases as the time elapses. The absolute value of the radial velocity in the near-wall region rapidly increases from τ^+=-21 to -10.5, corresponding to the downwash in the channel middle region. After that, $\hat{u}_r$ takes the same value at τ^+=0 and τ^+=-10.5 in the region near y/δ=0.2, whereas the estimated radial velocity begins to decrease near y/δ=0.4. Furthermore, a drastic decrease of the estimated radial velocity is observed at τ^+=10.5 and 21.

The time dependency of the estimated radial velocity on the concave side is shown in Fig. 14. In the second quadrant motion (Fig. 14(a)), the peak value of radial velocity is not observed in the channel middle region in contrast to that on the convex side. It is conjectured that the development of the second quadrant motion is more autonomic than that on the convex side. The radial velocity attains its peak value at τ^+=0. By

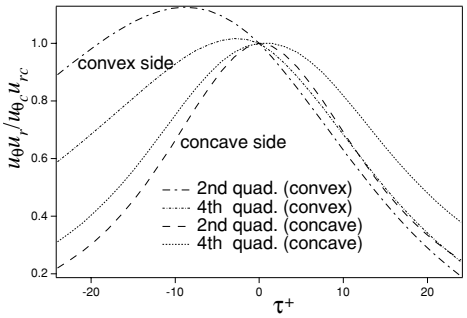

Fig. 15 Time dependency of estimated Reynolds shear stress $\hat{u}_\theta \hat{u}_r$ on the reference frame with convective velocity (x'^+=0 at τ^+=0, y^+=15, z'^+=0)

comparison between the curves at τ^+=-21 and τ^+=21, we notice that the decaying process is milder than the development process. This is attributed to the constraint of the second-quadrant decaying motion affected by the centrifugal force, which should enhance the second quadrant motion. A similar trend is observed in the case of fourth quadrant (Fig. 14(b)) except for the strengthened symmetry with respect to the time.

Figure 15 shows the time dependency of the estimated Reynolds shear stress $\hat{u}_\theta \hat{u}_r$ on the reference frame with the convective velocity at y^+=15 and z'=0. The Reynolds shear stress is normalized by that of the conditional velocities, i.e., $-u_{c\theta}u_{cr}$. A significant asymmetry with respect to the time appears on the convex side. Since the estimated streamwise velocity has the strong temporal symmetry (not shown here), this trend is mainly due to the significant asymmetry of the estimated radial velocity shown in Fig. 13. On the other hand, developing and decaying processes show relatively similar time dependency on the concave side. It is conjectured that the self-sustaining mechanism has more strong temporal symmetry.

CONCLUSIONS

DNS of turbulent curved channel flow is conducted to clarify the momentum transport mechanism of turbulent wall shear flow subjected to streamline curvature. The following conclusions can be drawn.

The radial turbulent intensity is enhanced as the curvature increases. The Richardson number distribution reveals that this is due to the extra production by the centrifugal effect.

On the concave side, there is an inherent mechanism which enhances the turbulent motion. This is clearly illustrated by the distribution of the quadrant contribution to the Reynolds stress. On the convex side, the turbulent motion is restrained.

Furthermore, the time development characteristics of the second- and fourth-quadrant motions are extracted by means of the spatio-temporal linear stochastic estimation. It is clarified that the development of turbulent production motion requires the large strong roll cell in the channel middle region against the centrifugal stabilizing effect on the convex side, although those vortices are not observed on the concave side. Moreover, the strong outflow or downwash induced by the roll cell in the channel middle region is confirmed prior to the occurrence of each second or fourth quadrant motion respectively.

ACKNOWLEDGMENT

This work was supported through the research project on "Micro Gas Turbine/Fuel Cell Hybrid-type Distributed Energy System" by the Department of Core Research for Evolutional Science and Technology (CREST) of the Japan Science and Technology Corporation (JST).

REFERENCES

Adrian, R. J., 1975, "On the Role of Conditional Averages in Turbulent Theory," Turbulence in Liquids, Sci. Press 54.

Bradshaw, P., 1969, "The analogy between streamline curvature and buoyancy in turbulent shear flow," *J. Fluid Mech.* **36**, 177.

Choi, H., Moin, P. and Kim, J., 1993, "Direct numerical simulation of turbulent flow over riblets," *J. Fluid Mech.* **255**, 503.

Eskinazi, S.&Yeh, H., 1956, "An investigation on fully developed turbulent flows in a curved channel," *J. Aero. Sci.* **23**, 23.

Kim, J. and Moin, P., 1985, "Application of a fractional-step method to incompressible Navier-Stokes equations," *J. Comput. Phys.* **59**, 308.

Moser, R.D. and Moin, P., 1987, "The effects of curvature in wall-bounded turbulent flows," *J. Fluid Mech.* **175**, 479.

Rayleigh, J. W. S., 1917, "On the dynamics of revolving fluids," *Proc. R. Soc. London*, **93A**, 148.

Wattendorf F.L., 1935, "A study of the effect of curvature on fully developed turbulent flow," *Proc. R. Soc. London* **148**, 565.